

Angle-resolved photoemission study of NbGeSb with non-symmorphic symmetry

Huan Ma(马欢), Ning Tan(谭宁), Xuchuan Wu(吴徐传), Man Li(李满), Yiyan Wang(王义炎), Hongyan Lu(路洪艳), Tianlong Xia(夏天龙), and Shancai Wang(王善才)

Citation: Chin. Phys. B, 2024, 33 (**2**): 027102. DOI: 10.1088/1674-1056/ad0ccf
Journal homepage: http://cpb.iphy.ac.cn; http://iopscience.iop.org/cpb

What follows is a list of articles you may be interested in

Electronic structure study of the charge-density-wave Kondo lattice $CeTe_3$

Bo Wang(王博), Rui Zhou(周锐), Xuebing Luo(罗学兵), Yun Zhang(张云), and Qiuyun Chen(陈秋云)
Chin. Phys. B, 2023, 32 (**9**): 097103. DOI: 10.1088/1674-1056/acb41e

Magnetic impurity in hybrid and type-II nodal line semimetals

Xiao-Rong Yang(杨晓容), Zhen-Zhen Huang(黄真真), Wan-Sheng Wang(王万胜), and Jin-Hua Sun(孙金华)
Chin. Phys. B, 2021, 30 (**6**): 067103. DOI: 10.1088/1674-1056/abfa02

Stiefel-Whitney classes and topological phases in band theory

Junyeong Ahn, Sungjoon Park, Dongwook Kim, Youngkuk Kim, Bohm-Jung Yang
Chin. Phys. B, 2019, 28 (**11**): 117101. DOI: 10.1088/1674-1056/ab4d3b

Structural, elastic, and electronic properties of topological semimetal

WC-type *MX* family by first-principles calculation

Sami Ullah, Lei Wang(王磊), Jiangxu Li(李江旭), Ronghan Li(李荣汉), Xing-Qiu Chen(陈星秋)
Chin. Phys. B, 2019, 28 (**7**): 077105. DOI: 10.1088/1674-1056/28/7/077105

Topological nodal line semimetals

Chen Fang(方辰), Hongming Weng(翁红明), Xi Dai(戴希), Zhong Fang(方忠)
Chin. Phys. B, 2016, 25 (**11**): 117106. DOI: 10.1088/1674-1056/25/11/117106

Angle-resolved photoemission study of NbGeSb with non-symmorphic symmetry

Huan Ma(马欢)[1,2], Ning Tan(谭宁)[1,2], Xuchuan Wu(吴徐传)[1,2], Man Li(李满)[3], Yiyan Wang(王义炎)[4], Hongyan Lu(路洪艳)[5,†], Tianlong Xia(夏天龙)[1,2,‡], and Shancai Wang(王善才)[1,2,§]

[1] *Department of Physics, Key Laboratory of Quantum State Construction and Manipulation (Ministry of Education), Renmin University of China, Beijing* 100872, *China*

[2] *Beijing Key Laboratory of Opto-Electronic Functional Materials & Micro-Nano Devices, Renmin University of China, Beijing* 100872, *China*

[3] *School of Information Network Security, People's Public Security University of China, Beijing* 100038, *China*

[4] *Institute of Physical Science and Information Technology, Anhui University, Hefei* 230601, *China*

[5] *School of Physics and Physical Engineering, Qufu Normal University, Qufu* 273165, *China*

(Received 22 September 2023; revised manuscript received 13 November 2023; accepted manuscript online 16 November 2023)

We investigate the electronic structure of NbGeSb with non-symmorphic symmetry. We employ angle-resolved photoemission spectroscopy (ARPES) to observe and identify the bulk and surface states over the Brillouin zone. By utilizing high-energy photons, we identify the bulk Fermi surface and bulk nodal line along the direction X–R, while the Fermi surface of the surface state is observed by using low-energy photons. We observe the splitting of surface bands away from the high-symmetry point $\overline{X}$. The density functional theory calculations on bulk and 1 to 5-layer slab models, as well as spin textures of NbGeSb, verify that the band splitting could be attributed to the Rashba-like spin–orbit coupling caused by space-inversion-symmetry breaking at the surface. These splitted surface bands cross with each other, forming two-dimensional Weyl-like crossings that are protected by mirror symmetry. Our findings provide insights into the two-dimensional topological and symmetry-protected band inversion of surface states.

Keywords: non-symmorphic symmetry, nodal line, splitting of surface bands, angle-resolved photoemission spectroscopy

PACS: 71.20.–b, 79.60.–i

DOI: 10.1088/1674-1056/ad0ccf

1. Introduction

Topological phases of matter witnessed significant advancements in recent decades.[1] These phases range from topological insulators to topological semimetals, including Dirac semimetals and Weyl semimetals.[2–4] The properties of these materials, such as dimensionality, degeneracy, slope, and the order of crossing in the bulk electronic structures, are governed by symmetry.[5] For instance, nodal points exist as zero-dimensional entities at discrete points in the Brillouin zone (BZ), nodal lines manifest as one-dimensional features along specific lines in the BZ, and nodal surfaces characterize two-dimensional (2D) structures found on particular planes in the BZ. Furthermore, the density of states (DOS) of low-energy excitations differs within these topological semimetals: nodal-line semimetals exhibit a higher DOS for low-energy excitations along their nodal lines, while nodal-surface semimetals possess a constant DOS near the nodal surfaces.[5]

Materials with nonsymmorphic structures, such as *WHM* family (W = Zr, Hf, or La, H = Si, Ge, Sn, or Sb, and M = O, S, Se, and Te),[6,7] have been proposed to be nodal line semimetals in the absence of spin–orbit coupling (SOC). This characteristic makes them promising candidates in practical applications of 2D topological insulators for heterostructural devices.[8] ZrSiS, being the most representative among these materials, has been thoroughly studied and found to possess extraordinary properties.[9–14] For instance, in the field of quantum transport, ZrSiS demonstrates nonsaturating magnetoresistance (MR), butterfly shape angular MR with rotating magnetization, and nontrivial Berry phase extracted from the Shubnikov–de Haas (SdH) oscillations.[9,11] Moreover, several Dirac cones form a Fermi surface (FS) with Dirac nodes protected by non-symmorphic symmetry, allowing for the coexistence of surface states alongside bulk state bands in ZrSiS.[10,13]

NbGeSb shares the same structure of ZrSiS, and exhibits a wide range of properties.[15,16] The MR behavior of NbGeSb follows a parabolic trend, reaching an MR value of approximately 18% at $T = 3$ K and $B = 14$ T.[17] Angular MR measurements display a two-fold rotation symmetry.[18,19] Additionally, a negative MR has been observed in a magnetic field below $B = 3$ T.[19] Hall measurements reveal that electron carriers dominate the transport behavior.[17] Furthermore, the analysis of SdH oscillations demonstrates a nontrivial Berry phase, providing evidence for the topological nature of NbGeSb.[18] The slab model calculations showed that

†Corresponding author. E-mail: hylu@qfnu.edu.cn

‡Corresponding author. E-mail: tlxia@ruc.edu.cn

§Corresponding author. E-mail: scw@ruc.edu.cn

© 2024 Chinese Physical Society and IOP Publishing Ltd

the Ge-terminated surface exhibits type-I and type-II Weyl points, while the Sb-terminated surface has only type-I Weyl point.[19,20] Another investigation focused on Nb-terminated slab models with varying numbers of layers (1, 2, 4, 6) identified a quadruple degenerate node near $\overline{\Gamma}$ as well as a topologically protected Dirac cone.[21]

In ZrSiS, there exist surface states originating from Zr and S, respectively. However, they are separated in energy. The NbGeSb is the aliovalent substitutions of Nb for Zr and Sb for S. With the substitution, it provides a possibility to manipulate the electronic properties, such as shifting the surface bands to create a band inversion of the surface bands. Furthermore, with the substitution of heavy elements, e.g., Sb for S, the SOC should be considered. Spin-polarized surface states have been reported on NbGeSb.[20] However, the detailed bulk state such as nodal lines needs to be studied with photon energy dependence, and the spin polarized surface states and band inversion deserve detailed investigation.

In this paper, we extend the investigation by utilizing both the soft x-ray and ultraviolet photon to study both the bulk states and surface states band structures of NbGeSb. We employ angle-resolved photoemission spectroscopy (ARPES), in conjunction with density functional theory (DFT) calculations and slab models of the bulk and surface states, to gain a comprehensive understanding of the electronic properties of NbGeSb. We separate the surface state from bulk state, and identify the existence of nodal lines. We find the Rashiba-like splitting of the surface states and the Weyl-like crossings, as well as an asymmetric gap opening.

2. Crystal structure

The crystal structure of NbGeSb is isostructural to ZrSiS,[15,16] and its unit cell and primitive cell are shown in Figs. 1(a) and 1(b), respectively. NbGeSb crystallizes in a tetragonal structure with space group No. 129 ($P4/nmm$) and belongs to the D_{4h}^7 point group. This space group is characterized by several symmetry operations, including a glide plane $\{M_z|\frac{1}{2}\frac{1}{2}0\}$, which is a mirror transformation along the $\hat{z}$ plane combined with a half-translation in the $\hat{x}+\hat{y}$ direction; two screw axes $\{C_{2x}|\frac{1}{2}00\}$ and $\{C_{2y}|0\frac{1}{2}0\}$, which are two-fold rotations about the $\hat{x}$ ($\hat{y}$) axes combined with a half-translation along the corresponding axis; a mirror M_{xy}; and inversion symmetries.[13] The lattice constants are $a = b = 3.75$ Å and $c = 8.30$ Å. In particular, the distance between Sb^1 and Sb^2 along the c-axis is larger than that between other atoms, indicating a weak van der Waals (vdW) bond between Sb layers. After cleavage, a Sb-terminated surface layer was exposed during the ARPES measurements.

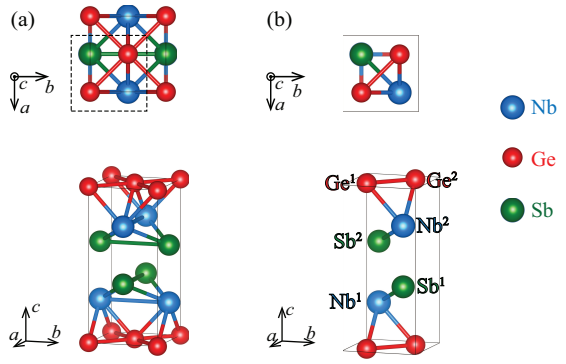


Fig. 1. Crystal structure of NbGeSb with space group $P4/nmm$ (No. 129, D_{4h}^7). (a) Unit cell. (b) Primitive cell. The upper row and lower row are top view and side view, respectively.

3. Methods

High quality single crystals of NbGeSb were grown by chemical vapor transport method.[17,18] Firstly, polycrystal of NbGeSb was prepared by the solid-state reaction. The mixtures of Nb, Ge and Sb powder were sealed in a quartz tube with a ratio of 1:1:1 and heated to 800 °C. Secondly, 10 mg/cm^3 of I_2 was used as transport agent to grow single crystals, and the temperature gradient was set as 950 °C–750 °C. The growth of single crystal was carried out in a two-zone furnace and lasted for three weeks.

ARPES measurements were performed at the Dreamline 09U beamline of Shanghai Synchrotron Radiation Facility (SSRF) that is equipped with Scienta-Omicron DA30L electron analyzer, beamline 13U of National Synchrotron Radiation Laboratory (NSRL) in Hefei and at Renmin University of China (RUC) both of which are equipped with Scienta-Omicron DA30 electron analyzers. The samples were cleaved *in situ*. During the measurements, the temperature was kept lower than $T = 36$ K, the vacuum was maintained better than 8×10^{-11} Torr, and the energy resolution was set better than 15 meV.

The electronic structure was studied by the first-principles calculations with the projector augmented wave (PAW) method[24,25] as implemented in the VASP package.[26–28] For the exchange–correlation function, the generalized gradient approximation (GGA) of the Perdew–Burke–Ernzerhof (PBE) formula[29] was adopted. The kinetic energy cutoff of the plane-wave basis was set to be 500 eV. The width of the Gaussian smearing method was 0.01 eV. The relaxation was stopped when the change of the total energy was smaller than 10^{-4} eV (10^{-5} eV) between two ionic steps for bulk (slab) calculations, and the energy convergence criterion was 10^{-11} eV (10^{-6} eV) for bulk (slab) calculations. A $26 \times 26 \times 12$ Γ-centered k-point mesh was utilized for the bulk BZ sampling while a $18 \times 18 \times 1$ for the slab BZ sampling. For slab calculations, five slab models along the c-axis with 1 to 5 layers were constructed, more than 20 Å vacuum thickness was adopted to eliminate the interactions of neighboring layers. The termination plane of slab models is the Sb atomic layer.

The crystal structure is visualized in the VESTA software.[30] The k-point mesh was generated by the VASPKIT software for the FS calculation,[31] and FSs are visualized in the FermiSurfer software.[32] The atomic-projection band structure is shown by the pymatgen code.[33–35] The primitive BZ and 2D BZ of the projected (001) surface of NbGeSb are shown in Fig. 2(b). For simplicity, we use Γ, X, M, etc. in the 3D BZ, while $\overline{\Gamma}$, $\overline{X}$, $\overline{M}$ notations in the 2D BZ.

4. Results

4.1. Nodal lines and nodal surfaces

The calculated bulk band structures of NbGeSb without and with SOC are depicted by black and red lines, respectively, in Fig. 2(a). A Dirac linear dispersion (i.e., a node), indicated by a green circle, is observed near E_F along the Γ–X direction. This Dirac node is protected by the C_{2v} symmetry along Γ–X line, a characteristic shared with similar materials like ZrSiS.[10] The Dirac node further forms a nodal line along k_z direction and at the $k_z = 0$ and $k_z = \pi$ planes in the BZ, forming a closed loop, as depicted by red dashed lines in Fig. 2(b). When taking SOC into account, a small gap opens at the node because the C_{2v} group allows only one irreducible representation,[10] as depicted by the red lines inside the green circle in Fig. 2(a).

In addition, as indicated by green square in Fig. 2(a), two bands are degenerate at energy $E - E_F \sim -1.15$ eV at the high-symmetry point X, which is protected by the non-symmorphic symmetry of the space group.[10] As presented by the black line in the figure, this degeneracy persists along the X–M direction. Additionally, as depicted by the red arrow in Fig. 2(c), the node undergoes variations in binding energy at different k_z planes, ranging from $k_z = 0$ to $k_z = \pi$. By analyzing the band dispersion along $\overline{X}$–$\overline{M}$ directions at different k_z planes, this Dirac-crossing forms a nodal surface at the BZ boundary, i.e., at the $k_x = \pi$ plane (indicated by the green plane in Fig. 2(b)) and the $k_y = \pi$ plane.[10,14] When the SOC is considered, the degeneracies along X–M directions are lifted except at the high symmetry point X, as indicated by the red lines in Fig. 2(a). The nodal surfaces at the $k_{x,y} = \pi$ planes transform into a nodal line along the X–R direction, as illustrated by the magenta line in Fig. 2(b).

4.2. Band structure with different photon energies

To examine the band dispersion of NbGeSb, we conducted ARPES measurements using several typical photon energies. The FSs and band dispersion along high symmetry lines are shown in Fig. 3. For comparison, a 3-layer slab calculation of FS topology and band dispersion with SOC is overlaid as solid curves on the top of the ARPES data.

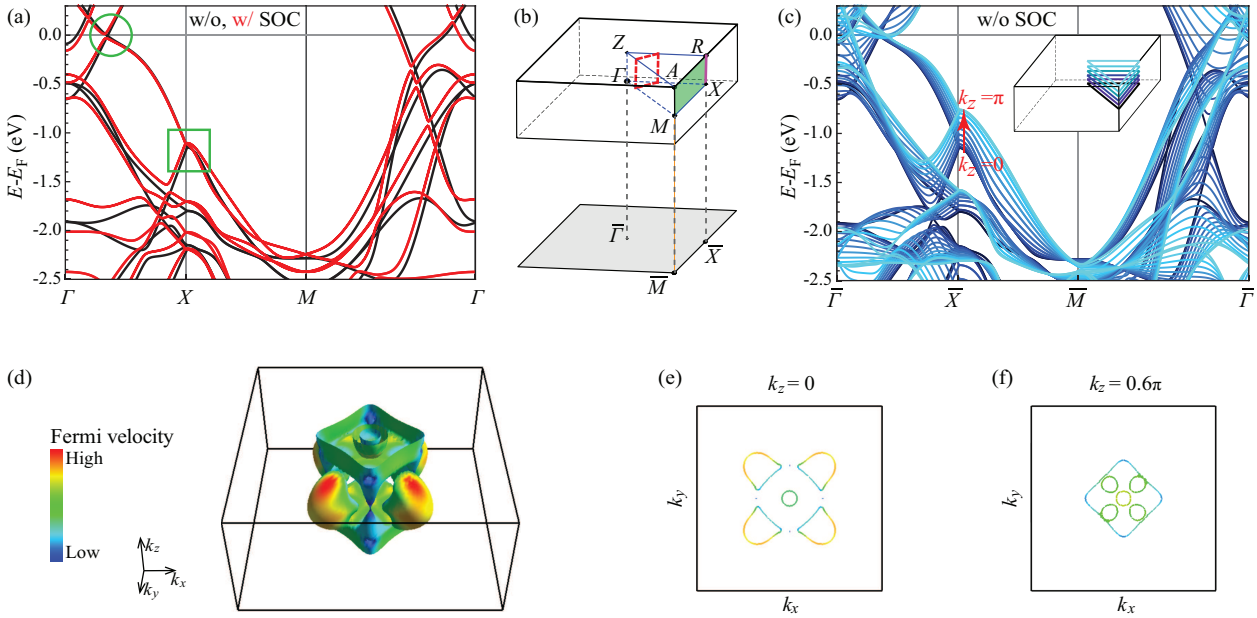


Fig. 2. (a) Calculated bulk band structure of NbGeSb without (w/o) and with (w/) SOC (black and red lines, respectively). Green circle indicates Dirac linear dispersion, and green square indicates node at X. (b) Primitive BZ (upper panel), and 2D BZ of the projected (001) surface (lower gray shaded areas). Without SOC, the locations of the nodal lines and nodal surfaces are labelled by red dashed lines and green planes. With SOC, the locations of the nodal lines are labelled by magenta lines. For simplicity, only 1/8 part of these are labelled in BZ. (c) Calculated bulk band structure without SOC along k-lines in the inset of BZ. Lines with colors from black to light cyan represent k-lines in different k_z-planes from $k_z = 0$ to $k_z = \pi$. Red arrow indicates the node at $\overline{X}$ shifts to lower binding energy from $k_z = 0$ plane to $k_z = \pi$ plane. (d) Calculated bulk FSs of NbGeSb without SOC. FSs at (e) $k_z = 0$ plane and (f) $k_z = 0.6\pi$ plane. Colors on FSs represent the Fermi velocity.

Compared with the calculated FSs of NbGeSb in Figs. 2(d)–2(f), the FSs measured with photon energies of 412 eV and 100 eV in Figs. 3(b) and 3(c) are more consistent with those of the $k_z = 0$ and $k_z = 0.6\pi$ planes, respectively. In Fig. 3(b) with high photon energy of 412 eV, the FSs of surface states mainly exist around the $\overline{\Gamma}$ point, while the FSs

around the $\overline{X}$ point have much weaker intensity. In comparison, ARPES with low photon energy of 100 eV reveals that the FSs around the $\overline{X}$ point have stronger intensity, as shown in Fig. 3(c). According to the universal curve of the photoelectrons' inelastic mean free path in Fig. 3(a), the photon is bulk sensitive at high energy of 412 eV, while it is surface sensitive at the energy of 20–100 eV. Combining the intensity variation with photon energy around the $\overline{X}$ point, the DFT band structures at different k_z planes in Fig. 2(c), and the slab calculations, we identify that the FSs around the $\overline{X}$ point are surface states. A high resolution mapping with photon energy of 20.5 eV is shown in Fig. 3(d). The surface states around the $\overline{X}$ exhibit two clear elliptical shapes, which agrees well with the slab calculations.

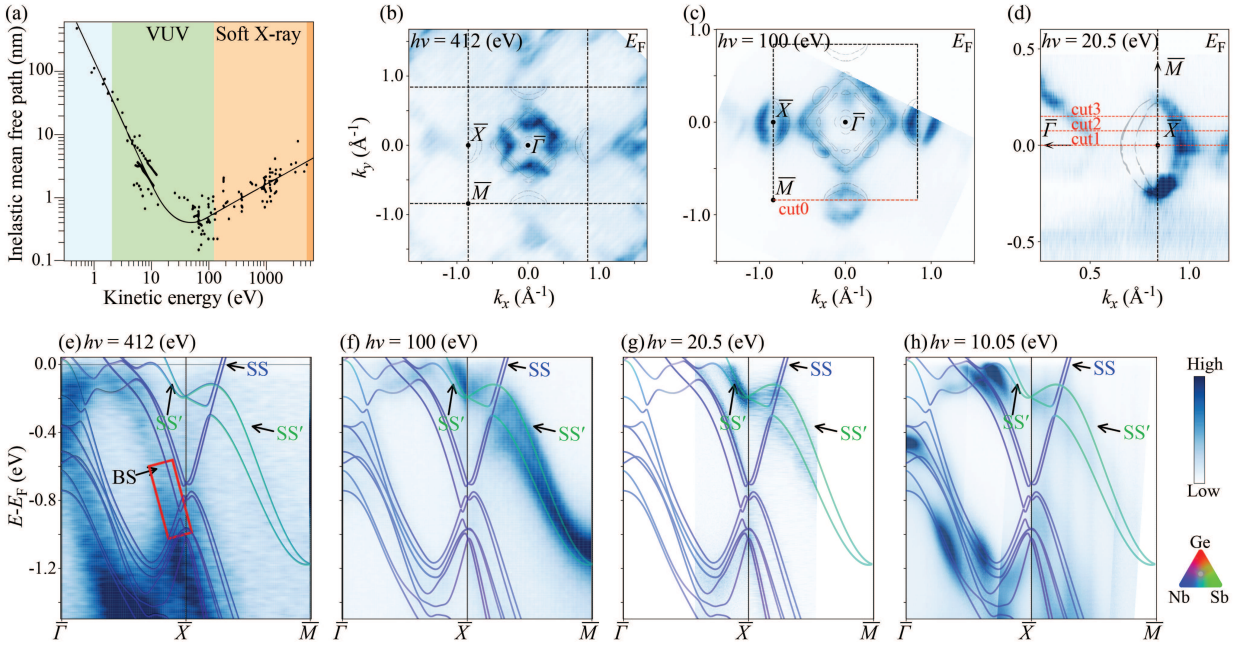


Fig. 3. (a) The universal curve of the photoelectrons' inelastic mean free path as a function of kinetic energy above the Fermi level.[22,23] (b)–(d) FSs measured with $h\nu = 412$ eV, 100 eV, 20.5 eV, respectively. (e)–(h) Band dispersions along the $\overline{\Gamma}$–$\overline{X}$–$\overline{M}$ line, measured with $h\nu = 412$ eV, 100 eV, 20.5 eV, 10.05 eV, respectively. Surface bands SS originating from Nb 4d-orbitals are labelled by blue color, while surface bands SS′ originating from Sb 5p-orbitals are labelled by green color. Red rectangle in (e) indicates the bands of bulk states (BS) measured with bulk sensitive high photon energy. For comparison, the 3-layer slab calculation with SOC is overlaid as solid curves on the top of the ARPES data. Calculated FSs are indicated by black curves, and calculated band structures are atomic projection.

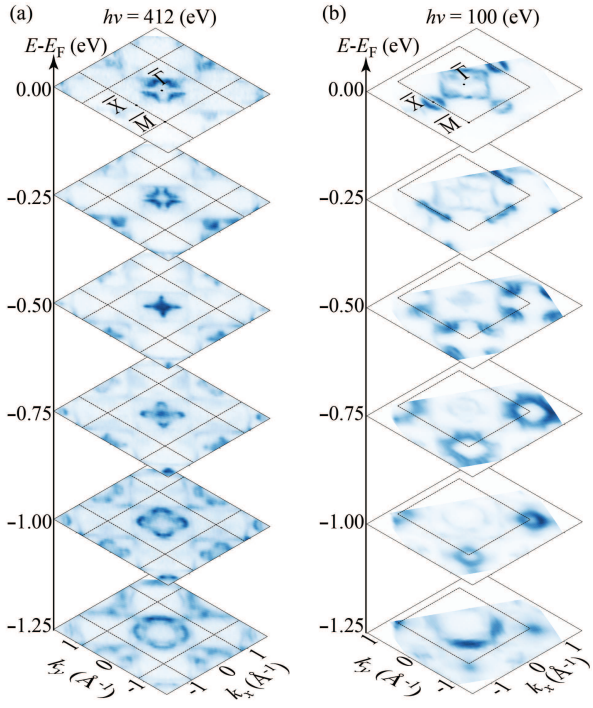


Fig. 4. Constant-energy ARPES intensity plots with (a) $h\nu = 412$ eV and (b) 100 eV, measured at energies from E_F to $E - E_F = -1.25$ eV.

To enhance the contrasts, constant energy intensity maps at various binding energies were obtained at photon energies of $h\nu = 412$ eV and 100 eV, as shown in Fig. 4. These maps reveal distinct features at different binding energies. At lower binding energies, particularly near E_F, the contrast is evident, showcasing the existence of surface states near the $\overline{X}$ point at $h\nu = 100$ eV, as well as the different intensity patterns at the BZ center. As we move to higher binding energies, e.g., approximately 1.25 eV below E_F, the surface states vanish and the constant energy plots of these two photon energies become more consistent.

Figures 3(e)–3(h) present the band dispersions along the high symmetry lines $\overline{\Gamma}$–$\overline{X}$–$\overline{M}$, measured with different photon energies: $h\nu = 412$ eV, 100 eV, 20.5 eV, and 10.05 eV, respectively. In Fig. 3(e) with bulk sensitive high photon energy of 412 eV, the bulk bands near $\overline{\Gamma}$ point are clearly visible with high intensity. Conversely, the bands of surface states have much weaker intensity at $\overline{X}$ point and along $\overline{X}$–$\overline{M}$ direction, where the blue and green calculated surface states bands are present. Notably, linear dispersions are observed in the red rectangle in Fig. 3(e), where the bulk bands exist in cal-

culations. These linear dispersions form a node at $\overline{X}$ point, in agreement with the bulk calculations in Fig. 2(a). To confirm this bulk state node, we conducted measurements with a range of high photon energies from $h\nu = 335$ eV to 495 eV, and show the integrated intensity at E_F as a function of the photon energy–$k_{\parallel}$ in Fig. 5(a). This intensity map shows a three-dimensional (3D) FS in the $k_{\parallel}$–k_z plane, indicating the bulk nature of these bands. Figure 5(b) provides confirmation of the bulk state nodes at the $\overline{X}$ point. These nodes are observed with photon energies ranging from 335 eV to 365 eV, and the variation of the Dirac-crossing in energy offers an evidence of the existence of the bulk nodal line along X–R, as indicated by the magenta lines in Fig. 2(b). At a photon energy of 10.05 eV, which is also bulk sensitive according to the universal curve, the enhancement of the bulk states and the suppression of the surface states are clearly seen in Fig. 3(h). In comparison, the surface states are clearly visible with enhanced intensity at $h\nu = 100$ eV and 20.5 eV, as demonstrated in Figs. 3(f) and 3(g).

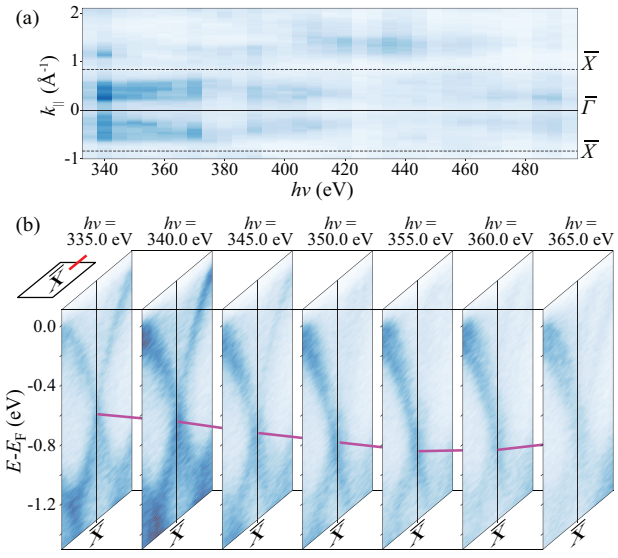


Fig. 5. (a) The photon energy–$k_{\parallel}$ intensity map along the $\overline{\Gamma}$–$\overline{X}$ plane in BZ. (b) Band dispersions with different photon energies along the red line shown in inset of BZ. Magenta lines indicate nodal line along $\overline{X}$–$\overline{R}$.

4.3. Surface state band splitting

According to the atomic-projection of band dispersions from slab calculation, the surface bands SS originate from Nb 4d-orbitals, while the surface bands SS′ originate from Sb 5p-orbitals. Sharing the same structure with ZrSiS and with aliovalent substitution of Nb for Zr and Sb for S, NbGeSb hosts symmetry protected nodal lines and corresponding surface states that are similar to ZrSiS.[10] In ZrSiS, the surface state SS originating from Zr locates at energy $E - E_F \sim -0.4$ eV, while the surface state SS′ originating from S locates at energy $E - E_F \sim -1.7$ eV.[13] In NbGeSb, due to the fact that Sb has one less valence electron than S, while Nb has one more electron than Zr, the corresponding surface state bands SS and SS′ in NbGeSb shift toward each other. Eventually, these bands cross each other, resulting in a band inversion, and form the band crossings in the vicinity of E_F, as shown in Fig. 3(f).

Now we focus on the band structure around $\overline{X}$ point. We present the experimental band dispersion along cut0–cut3 in Figs. 6(a) and 6(b), and the calculated 3D surface state band dispersion in Fig. 6(c). By extracting the peak position along $\overline{X}$–$\overline{M}$ (indicated by the blue and green dots) in Fig. 6(a), clear band splittings of SS and SS′ are observed. This observation is consistent with the slab calculations, which are overlayed as green and blue solid lines. From the atomic orbital-projection DFT calculations presented in Figs. S1–S8, the surface state bands arise predominantly from the outermost Sb layer and the top Nb layer. Additionally, by comparing DFT calculations of slab models with different layers, without and with SOC, in Fig. S9, we find that the SOC is crucial in producing the observed band splittings, while simply increasing the number of stacked layers can not drive the splitting of the bands in the slab models.

In Fig. 6(b), we present the band dispersion along the high symmetry line $\overline{\Gamma}$–$\overline{X}$ (cut1) and the parallel lines away from higy symmetry point $\overline{X}$ (cut2 and cut3). These band structures exhibit specific characteristics. One is that the bands are degenerate at $\overline{X}$ point at energy $E - E_F \sim -0.2$ eV and -0.7 eV (cut1), respectively. Another is that the degeneracies are lifted away from $\overline{X}$ along $\overline{X}$–$\overline{M}$ direction (cut2 and cut3). The surface state bands along $\overline{X}$–$\overline{M}$ have mirror parity, as shown in Figs. S1–S8. Along $\overline{X}$–$\overline{M}$ direction that is parallel to the k_y-axis, as shown in Figs. S1(a) and S2(c), the bands SS consist of Nb orbitals $\{d_{yz}, d_{x^2-y^2}, d_{z^2}\}$ which are even under M_x ($x \to -x$), while bands SS′ consist of Nb orbitals $\{d_{xy}, d_{xz}\}$ which are odd under M_x. In addition, as depicted in Figs. S3(a) and S4(c), bands SS′ has contribution from Sb p_z-orbital, which is also odd under M_x if an addition Bloch phase factor $e^{ik\cdot r}$ from the relative position between Nb and Sb is considered.[20]

Such mirror symmetry observed in the electronic band structure is also reflected in spin textures. We calculate the spin textures corresponding to bands #3 and #4 in Fig. 6(a), and display them in Figs. 6(d) and 6(e). Along several high symmetry lines with mirror symmetry, $\overline{\Gamma}$–$\overline{X}$, $\overline{X}$–$\overline{M}$, and $\overline{\Gamma}$–$\overline{M}$, the spin textures are perpendicular to these mirror lines, as shown in Fig. 6(d). Furthermore, as shown in Fig. 6(e), the inner FS and the outer FS around the $\overline{X}$ point exhibit opposite spin polarizations. This observed surface state band splitting, together with the calculated spin textures, could be attributed to the Rashba-like splitting, which is caused by a space-inversion-symmetry breaking at the surface.[20,36] In comparison, Rashba-like splitting is negligible in ZrSiS, probably due to the lighter atomic mass of S than that of Sb in NbGeSb and the resultant smaller SOC in ZrSiS.[10,13,37]

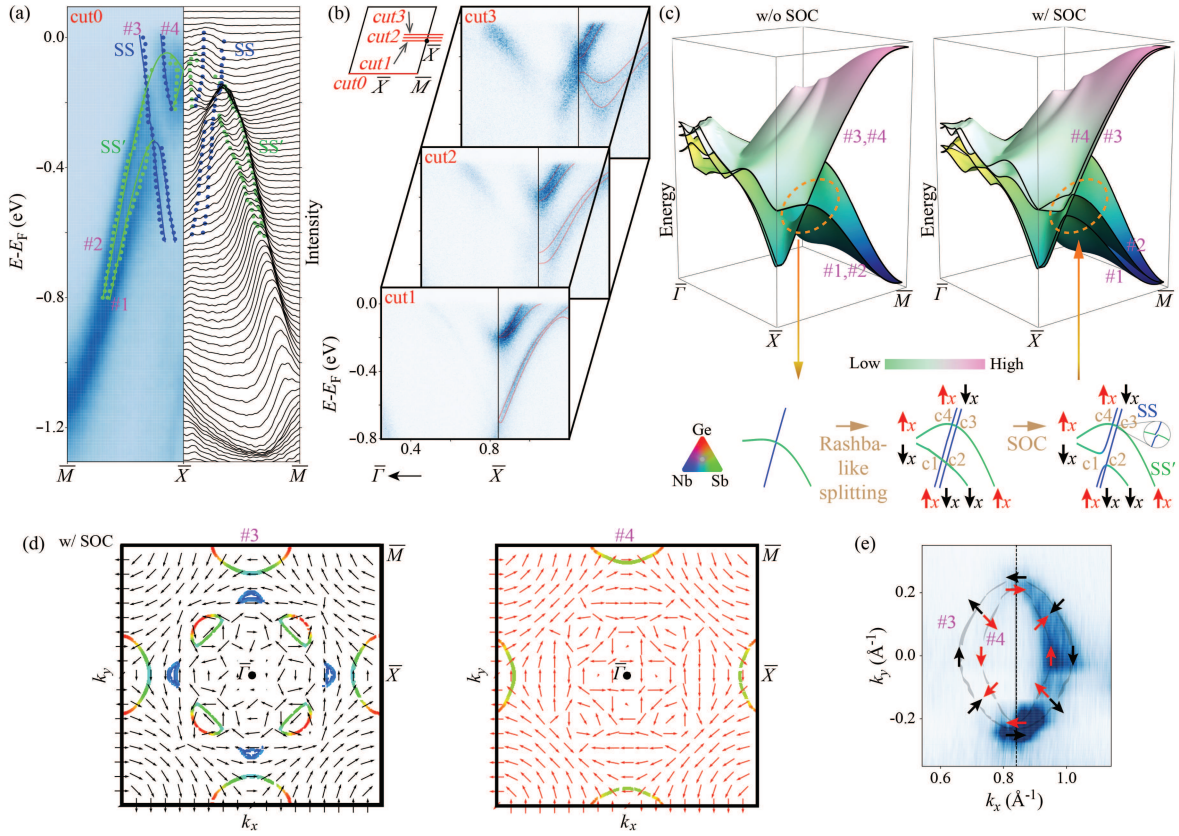


Fig. 6. (a) Band dispersions and MDC along cut0 ($\bar{M}$–$\bar{X}$–$\bar{M}$) in Fig. 3(c). Surface state bands SS and SS′, labeled from #1 to #4 in magenta font, are extracted from MDC as blue and green colors. (b) Band dispersions along cut1–3 in Fig. 3(d). For comparison, the 3-layer slab calculation with SOC is overlaid as red dashed curves on the top of the ARPES data. The paths of dispersions in (a) and (b) are also marked by red lines in the inset of BZ. (c) Calculated 3D surface band structure of 3-layer Sb-terminated slab model of NbGeSb. Surface states of the bands #1–#4 are shown in left panel (without SOC) and right panel (with SOC). Lower panel shows how surface state band structure changes considering the Rashba-like splitting and SOC.[20] The contribution from Nb 4d-orbitals are labelled by blue color, and contribution from Sb 5p-orbitals is labelled by green color. (d) Calculated spin textures of bands #3 and #4, respectively, and (e) the spin texture on FSs of bands #3 (black) and #4 (red), respectively, around the $\bar{X}$ point.

As shown in the lower panel of Fig. 6(c), after Rashba-like splitting, there are four crossings (labeled as c1 to c4). Considering the spin textures, crossings c2 and c4 occur between bands with the same spin polarization, while crossings c1 and c3 occur between bands with opposite spin polarizations. One of these mirror protected crossings c4 exhibits a band inversion between the spin-polarized states, resulting in a Weyl-like crossing. This band inversion is caused by the intrinsic band inversion of surface state. Analysis through the tight-binding model, with consideration of the spin–orbital interaction, reveals that at crossing c1, the change in spin between the bands is opposite to their change in orbital angular momentum. As a result, a gap opens at this crossing.[20] However, at crossing c3, the change in spin between the bands aligns with their change in angular momentum, resulting in a negligible gap.[20]

5. Conclusion

In summary, we investigate the electronic structure of NbGeSb by using ARPES and DFT bulk and slab calculations. By using different photon energies and DFT calculations, we identify the existence of bulk nodal line along high symmetry line X–R, and the existence of surface states originating from Nb and Sb atoms. In comparison with ZrSiS, the surface bands shift toward each other, eventually crossing and causing a band inversion. We observe splitting of surface bands which could be attributed to the Rashba-like SOC, caused by space-inversion-symmetry breaking at the surface. The analysis of spin polarization projections reveals asymmetric gaps among band crossings, and the formation of Weyl-like points protected by mirror symmetry. NbGeSb provides a unique platform for studying the topological and symmetry-protected band inversion of surface state, contributing to our understanding of the electronic properties of this material.

Acknowledgements

Project supported by the National Key Research and Development Program of China (Grant No. 2022YFA1403803). H. M. is supported by the Fundamental Research Funds for the Central Universities, and the Research Funds of Renmin University of China (Grant No. 22XNH099). The results of DFT calculations described in this paper are supported by HPC Cluster of ITP-CAS. M. L. is supported by the National Natural Science Foundation of China (Grant No. 12204536),

the Fundamental Research Funds for the Central Universities, and the Research Funds of People's Public Security University of China (PPSUC) (Grant No. 2023JKF02ZK09). T. L. X. is supported by the National Key R&D Program of China (Grant No. 2019YFA0308602) and the National Natural Science Foundation of China (Grant Nos. 12074425 and 11874422). Y. Y. W. is supported by the National Natural Science Foundation of China (Grant No. 12104011). H. Y. L. is supported by the National Natural Science Foundation of China (Grant No. 12074213), the Major Basic Program of Natural Science Foundation of Shandong Province (Grant No. ZR2021ZD01), and the Project of Introduction and Cultivation for Young Innovative Talents in Colleges and Universities of Shandong Province.

References

[1] Wen X G 2017 *Rev. Mod. Phys.* **89** 041004
[2] Hasan M Z and Kane C L 2010 *Rev. Mod. Phys.* **82** 3045
[3] Qi X L and Zhang S C 2011 *Rev. Mod. Phys.* **83** 1057
[4] Armitage N P, Mele E J and Vishwanath A 2018 *Rev. Mod. Phys.* **90** 015001
[5] Lv B Q, Qian T and Ding H 2021 *Rev. Mod. Phys.* **93** 025002
[6] Xu Q, Song Z, Nie S, Weng H, Fang Z and Dai X 2015 *Phys. Rev. B* **92** 205310
[7] Zhao Y X and Schnyder A P 2016 *Phys. Rev. B* **94** 195109
[8] Lou R, Ma J Z, Xu Q N, Fu B B, Kong L Y, Shi Y G, Richard P, Weng H M, Fang Z, Sun S S, Wang Q, Lei H C, Qian T, Ding H and Wang S C 2016 *Phys. Rev. B* **93** 241104
[9] Ali M N, Schoop L M, Garg C, Lippmann J M, Lara E, Lotsch B and Parkin S S P 2016 *Science Advances* **2** e1601742
[10] Schoop L M, Ali M N, Straßer C, Topp A, Varykhalov A, Marchenko D, Duppel V, Parkin S S P, Lotsch B V and Ast C R 2016 *Nat. Commun.* **7** 11696
[11] Wang X, Pan X, Gao M, Yu J, Jiang J, Zhang J, Zuo H, Zhang M, Wei Z, Niu W, Xia Z, Wan X, Chen Y, Song F, Xu Y, Wang B, Wang G and Zhang R 2016 *Advanced Electronic Materials* **2** 1600228
[12] Lodge M S, Chang G, Huang C Y, Singh B, Hellerstedt J, Edmonds M T, Kaczorowski D, Hosen M M, Neupane M, Lin H, Fuhrer M S, Weber B and Ishigami M 2017 *Nano Lett.* **17** 7213
[13] Topp A, Queiroz R, Grüneis A, Müchler L, Rost A W, Varykhalov A, Marchenko D, Krivenkov M, Rodolakis F, McChesney J L, Lotsch B V, Schoop L M and Ast C R 2017 *Phys. Rev. X* **7** 041073
[14] Fu B B, Yi C J, Zhang T T, Caputo M, Ma J Z, Gao X, Lv B Q, Kong L Y, Huang Y B, Richard P, Shi M, Strocov V N, Fang C, Weng H M, Shi Y G, Qian T and Ding H 2019 *Science Advances* **5** eaau6459
[15] Johnson V and Jeitschko W 1973 *Journal of Solid State Chemistry* **6** 306
[16] Tremel W and Hoffmann R 1987 *J. Am. Chem. Soc.* **109** 124
[17] Guo L, Zhao W, Ding N, Shi X Y, Xu M, Chen L, Gao G Y, Dong S and Zheng R K 2020 *J. Phys.: Condens. Matter* **32** 435701
[18] Murphy K 2020 *Quantum oscillation studies in the unconventional superconductor YFe_2Ge_2 and in the Dirac semimetal candidates NbXSb (X = Ge/Si)* Ph. D. thesis (University of Cambridge)
[19] Shao J 2020 *Study on First Principle and Electrical Transport of Topological Materials NbGeSb and KHgSb* Master's thesis (Harbin Institute of Technology)
[20] Marković I, Hooley C A, Clark O J, Mazzola F,Watson M D, Riley J M, Volckaert K, Underwood K, Dyer M S, Murgatroyd P A E, Murphy K J, Fèvre P L, Bertran F, Fujii J, Vobornik I, Wu S, Okuda T, Alaria J and King P D C 2019 *Nat. Commun.* **10** 5485
[21] Li W, Song J, Qin Y, Qin P, Ren R, Wang Y, Bai X, Yang X and Cao C 2022 *Phys. Lett. A* **446** 128277
[22] Seah M P and Dench W A 1979 *Surface and Interface Analysis* **1** 2
[23] Zhang H, Pincelli T, Jozwiak C, Kondo T, Ernstorfer R, Sato T and Zhou S 2022 *Nature Reviews Methods Primers* **2** 54
[24] Bločhl P E 1994 *Phys. Rev. B* **50** 17953
[25] Kresse G and Joubert D 1999 *Phys. Rev. B* **59** 1758
[26] Kresse G and Hafner J 1993 *Phys. Rev. B* **47** 558
[27] Kresse G and Furthmuller J 1996 *Computational Materials Science* **6** 15
[28] Kresse G and Furthmuller J 1996 *Phys. Rev. B* **54** 11169
[29] Perdew J P, Burke K and Ernzerhof M 1996 *Phys. Rev. Lett.* **77** 3865
[30] Momma K and Izumi F 2011 *Journal of Applied Crystallography* **44** 1272
[31] Wang V, Xu N, Liu J C, Tang G and Geng W T 2021 *Computer Physics Communications* **267** 108033
[32] Kawamura M 2019 *Computer Physics Communications* **239** 197
[33] Jain A, Hautier G, Moore C J, Ping Ong S, Fischer C C, Mueller T, Persson K A and Ceder G 2011 *Computational Materials Science* **50** 2295
[34] Ong S P, Richards W D, Jain A, Hautier G, Kocher M, Cholia S, Gunter D, Chevrier V L, Persson K A and Ceder G 2013 *Computational Materials Science* **68** 314
[35] Jain A, Ong S P, Hautier G, Chen W, Richards W D, Dacek S, Cholia S, Gunter D, Skinner D, Ceder G and Persson K A 2013 *APL Materials* **1** 011002
[36] Takane D, Wang Z, Souma S, Nakayama K, Trang C X, Sato T, Takahashi T and Ando Y 2016 *Phys. Rev. B* **94** 121108
[37] Neupane M, Belopolski I, Hosen M M, Sanchez D S, Sankar R, Szlawska M, Xu S Y, Dimitri K, Dhakal N, Maldonado P, Oppeneer P M, Kaczorowski D, Chou F, Hasan M Z and Durakiewicz T 2016 *Phys. Rev. B* **93** 201104